Continental Shelf Research 60S (2013) S22–S29

Contents lists available at SciVerse ScienceDirect

Continental Shelf Research

journal homepage: www.elsevier.com/locate/csr

Wave mixed, wind-generated near-surface shear observed over a tidal flat

Stephen M. Henderson [a,*], Julia C. Mullarney [b]

[a] School of the Environment, Washington State University, Vancouver, 14204 Salmon Creek Ave, Vancouver, WA 98686, United States
[b] Department of Earth and Ocean Sciences, University of Waikato, Private Bag 3105, Hamilton 3240, New Zealand

ARTICLE INFO

Article history:
Received 3 April 2011
Received in revised form
3 May 2012
Accepted 12 May 2012
Available online 23 May 2012

Keywords:
Waves
Breaking
Mixing
Shear
Turbulence
Turbulence closure models

ABSTRACT

Around high tide over a flooded tidal flat, vertical shear measured 0.13–0.4 m beneath the sea surface by upward-looking Acoustic Doppler Profilers (ADPs) was usually aligned with the wind. However, shear did not increase with increasing windspeed, likely owing to an increase in wave heights and wave-generated mixing with increasing windspeed. The associated increase in water-side drag coefficient with windspeed was predicted, with substantial scatter, by a model for near-surface mixing by breaking waves. A depth-independent eddy-viscosity model yielded only slightly less skill than a fitted depth-dependent model. Farther (0.3–0.6 m) from the surface, model skill was low, suggesting that shear at depth was often determined by factors other than wind. Wave heights tended to increase with increasing water depth. Consequently, the simulated wave-generated surface eddy viscosity tended to increase with increasing depth.

Published by Elsevier Ltd.

1. Introduction

Breaking waves and wave–current interactions generate turbulence near the ocean surface, creating a Wave Affected Surface Layer (WASL) characterized by rapid mixing (Donelan, 1998; Thorpe, 2004). This WASL, which in the open ocean often extends a few meters beneath the surface, mediates air–sea fluxes of chemicals, momentum, and heat (Melville, 1996; Gerbi et al., 2008). In shallow beach (Feddersen et al., 2007) and estuarine (Jones and Monismith, 2008) environments, the WASL can extend through most of the water column. Observations over tidal flats are lacking, but shallow depths suggest that the WASL might play a significant role in mixing.

Most observations of the WASL have focused on quantifying the rapid dissipation of turbulent energy injected by surface breakers (Kitaigorodskii et al., 1983; Anis and Moum, 1992; Terray et al., 1996; Gerbi et al., 2009). Craig and Banner (1994) and Burchard (2001) developed two-equation turbulence closures that are consistent with the observed depth-dependence of turbulent dissipation rates (although the data show significant scatter). Fewer observational studies have focused on shear ($\partial u/\partial z$, where u is the horizontal velocity in wind direction, z is the depth beneath surface) in the WASL, but such shear might be important to the transport and dispersion of buoyant pollutants and organisms (Elliot, 1986). Model–data comparisons using two-equation turbulence closures, in depths of 2–12 m (Stacey and Pond, 1997; Stacey, 1999) and 1–47 m (Terray et al., 1999) beneath the surface, indicate that velocity-profile predictions are improved if wave-enhanced mixing is simulated. These models were not tested against shear less than about 1 m from the water surface.

The depth-dependence of wave-generated eddy viscosity has not been measured. Two-equation turbulence closures indicate that the depth dependence of turbulent viscosity is determined by the competing effects of dissipation and turbulent length scale: the decrease in turbulent dissipation with depth would lead to decreased mixing with depth, if it were not for a coincident increase in length scale that acts to increase mixing. Unlike depth dependence of dissipation, depth dependence of turbulent length scale has not been widely measured.

Here, models for shear in the WASL (Section 2) are tested against measurements of near-surface (z=0.13–0.60 m) shear over the tidal flats of Skagit Bay, Washington (Section 3). Within an hour of high tide, tidal currents were weak and near-surface shear was usually aligned with the wind, indicating that much of the shear was wind-generated (Section 4). However, near-surface shear did not consistently increase with increasing windspeed. This result was explained by an increase in wave height and mixing with windspeed. Models for wave-generated mixing fitted the relationship between wind stress and near-surface shear better than a rigid-surface model that neglected wave-generated mixing, although scatter about model predictions was substantial. Results are summarized in Section 5.

* Corresponding author. Tel.: +1 360 546 9268.
E-mail addresses: steve_henderson@vancouver.wsu.edu, steve_henderson@wsu.edu (S.M. Henderson), juliam@waikato.ac.nz (J.C. Mullarney).

0278-4343/$ - see front matter Published by Elsevier Ltd.
http://dx.doi.org/10.1016/j.csr.2012.05.008

2. Models for near-surface mixing

2.1. Shear, drag coefficient, and eddy viscosity

Two parameters are often used to relate stress to velocity profiles: the eddy viscosity, which is used in most turbulence models, and the drag coefficient, which is most easily related to observations.

The eddy viscosity ν is defined by

$$u_*^2 = -\nu \frac{\partial u}{\partial z}, \tag{1}$$

where u is the mean downwind water velocity, the water-side friction velocity $u_* = (\tau/\rho)^{1/2}$, τ is the wind stress, ρ is the water density, and we have used the equality between the wind stress and the shear stress immediately below the wave-trough elevation. The minus sign in Eq. (1) results from choosing z to be positive downward.

The drag coefficient C for friction between depths z_1 and z_2 (with $z_2 > z_1$) is defined by $\tau = \rho C \Delta u^2$, or equivalently

$$u_* = C^{1/2} \Delta u, \tag{2}$$

where $\Delta u = u(z_1) - u(z_2)$. The drag coefficient depends on the locations z_1 and z_2, and quantifies mixing between these locations. Integrating Eq. (1) from z_1 to z_2 and comparing with Eq. (2) yields

$$C^{1/2} = \left(\int_{z_1}^{z_2} \frac{u_* \, dz}{\nu} \right)^{-1}. \tag{3}$$

The purpose of this paper is to compare observations of the relationship between u_* and Δu (i.e., observations of $C^{1/2}$) over a tidal flat with predictions obtained by substituting eddy-viscosity models into Eq. (3). All the eddy viscosity models tested take the form

$$\nu = S_M q l, \tag{4}$$

where the empirical dimensionless parameter $S_M \approx 0.39$ in unstratified boundary layers (Craig and Banner, 1994), q is a turbulent velocity scale ($2^{1/2}$ times the square root of turbulent kinetic energy), and l is a turbulent length scale. Next, eddy viscosity models are introduced.

2.2. Rigid surface model

Neglecting wave-generated turbulence and assuming that near-surface flow is equivalent to flow under a rigid surface leads to (Tennekes and Lumley, 1972)

$$\nu = \kappa u_* z, \tag{5}$$

where the empirical dimensionless parameter $\kappa = 0.4$. The velocity profile is logarithmic and [from (3) and (5)] the drag coefficient is given by

$$C_r^{1/2} = \kappa / \log(z_2/z_1). \tag{6}$$

Open ocean observations (Terray et al., 1996, 1999; Gerbi et al., 2008) indicate that this rigid surface model performs poorly near the surface, but may perform well beneath the WASL.

2.3. Surface eddy-viscosity model

Unlike the rigid-surface model (Section 2.2), models for wave-enhanced mixing (described in detail in Section 2.4) predict a non-zero surface eddy viscosity ν_0. If the surface eddy viscosity depends on only u_*, the significant wave height Hs, and the wave phase speed c, then dimensional consistency requires

$$\nu_0 = \alpha_0 u_* Hs, \tag{7}$$

where α_0 is an unknown function of c/u_*. The corresponding near-surface velocity profile is linear, and the drag coefficient is given by

$$C_0^{1/2} = \frac{\alpha_0 Hs}{z_2 - z_1}. \tag{8}$$

The next section will discuss turbulence closures, and will propose

$$\alpha_0 = \alpha_0' w_a^{1/3}, \tag{9}$$

where the dimensionless wave age $w_a = c/u_{*a}$, the air-side friction velocity $u_{*a} = (\rho/\rho_a)^{1/2} u_*$, ρ_a is the air density, and the constant α_0' will be determined by fitting observations.

2.4. Turbulence closure models for depth-dependent eddy viscosity

To relate model (4) for mixing (which requires knowledge of the turbulent velocity q) to the turbulent dissipation rate ϵ (which is more commonly measured), we use the relationship

$$\epsilon = \frac{q^3}{Bl}, \tag{10}$$

where the empirical parameter $B \approx 16.6$ (Craig and Banner, 1994). From (4) and (10)

$$\nu = S_M B^{1/3} \epsilon^{1/3} l^{4/3}. \tag{11}$$

To predict mixing, it remains to specify l and ϵ. Following previous researchers (Drennan et al., 1992; Anis and Moum, 1992; Terray et al., 1996, 1999; Gemmrich and Farmer, 2004; Gerbi et al., 2009), we express depth-dependence in the form

$$l = \alpha_l Hs \zeta^{\beta_l}, \tag{12}$$

$$\epsilon = \frac{\alpha_\epsilon u_*^3}{Hs} \zeta^{\beta_\epsilon}, \tag{13}$$

where $\zeta = z/Hs$, and the empirical dimensionless parameters α_l, α_ϵ, β_l, and β_ϵ depend on depth. Fitting (Terray et al., 1999) suggests α_l is order-one and β_l ranges from 0 for $\zeta \ll 1$ to 1 for $\zeta \gg 1$. We assume wave generation by the wind scales as $u_*^2 c$, although scaling may transition to u_*^3 for large wave ages (Terray et al., 1996). Now, balance between wave generation and depth-integrated turbulent dissipation yields $\alpha_\epsilon \approx \alpha_\epsilon' w_a$, where α_ϵ' is an order-one constant (Terray et al., 1996 found $\alpha_\epsilon' \approx 0.3$ for young waves). In sufficiently deep water, the thickness of the WASL ζ_w may be roughly 10–20, possibly dependent on wave age (Terray et al., 1996). For $1 \lesssim \zeta \lesssim \zeta_w$, experiments have found a range of β_ϵ values, with $-2 < \beta_\epsilon < -3$ most common (Drennan et al., 1992; Anis and Moum, 1992; Terray et al., 1996; Gerbi et al., 2009), indicating a rapid decay in turbulence with distance from the surface location of breaking. Finite, non-zero ϵ requires $\beta_\epsilon \to 0$ as $\zeta \to 0$, although there does appear to be some increase in dissipation between wave trough and wave crest elevations (Gemmrich and Farmer, 2004). For $\zeta \gtrsim \zeta_w$, local shear production dominates wave-injected turbulence, so $\beta_\epsilon = -1$ and α_ϵ is no-longer determined by wind dissipation. The near-surface limit ($\beta_l = \beta_\epsilon = 0$) corresponds to the surface viscosity model of Section 2.3, whereas the large-depth limit $\beta_l = 1$, $\beta_\epsilon = -1$ corresponds to the rigid surface model of Section 2.2.

Combining (11)–(13) yields a depth-dependent wave-influenced eddy viscosity

$$\nu = \alpha_\nu u_* Hs \zeta^{\beta_\nu}, \tag{14}$$

where

$$\alpha_\nu = \alpha_\nu' w_a^{1/3}, \tag{15}$$

$$\beta_\nu = (\beta_\epsilon + 4\beta_l)/3, \tag{16}$$

and the constant

$$\alpha'_v = S_M(B\alpha'_\epsilon\alpha_l^4)^{1/3}. \tag{17}$$

From Eq. (16), the depth-dependence of dissipation ($\beta_\epsilon < 0$) and length scale ($\beta_l > 0$) have counteracting effects on the depth-dependence of eddy viscosity. From (14) and (3), the depth-dependent drag coefficient is given by

$$C_w^{1/2} = \frac{\alpha_v(1-\beta_v)}{\zeta_2^{1-\beta_v} - \zeta_1^{1-\beta_v}} \tag{18}$$

(where $\zeta_j = z_j/Hs$), which reduces to expressions (8) and (6) for surface and rigid models in the appropriate limits ($\beta_l \to 0$, $\beta_\epsilon \to 0$, $\beta_v \to 0$ for surface, $\beta_l \to 1$, $\beta_\epsilon \to -1$, $\beta_v \to 1$ for rigid).

3. Field site, instrumentation, and data analysis

Skagit Bay is a mesotidal bay within northern Puget Sound, Washington (Fig. 1a and b). The North Fork of the Skagit River (visible in the top right of Fig. 1c) and several distributary channels enter the eastern side of the bay. Once these channels reach the broad (about 4.5 km wide) tidal flats, they split into a braided network of shallow (<1 m deep) subtidal channels (Fig. 1c).

During 2008, two 2-MHz Nortek Aquadopp Acoustic Doppler Profilers (ADPs) were deployed in standard (not pulse-coherent) mode on the tidal flats 400–500 m from the shore, where depths ranged tidally from 0 to 2.4 m (14 days, instruments 1 and 2, Fig. 1c). During 2009, one identical ADP was deployed in standard mode, 80 m from shore, in a location sheltered by saltmarshes to the north and east where depths ranged from 0 to 1.8 m (11 days, instrument 3, Fig. 1c). Velocities were recorded in 0.1 m rangebins every 10 s (20 s for instrument 3) and subsequently filtered with a 16-min moving average. The final 8 days of data from ADP 2 were lost owing to accumulation of seaweed over the instrument.

Two additional Aquadopp ADPs were deployed (collocated with ADP 2 in 2008 and 20 m northwest of ADP 3 in 2009, Fig. 1c) in pulse-coherent mode, and recorded pressure at wave-resolving frequencies (8 Hz in 2008 and 4 Hz in 2009). These pulse-coherent instruments resolved waves but, owing to range limitations, did not measure shear or turbulence near the surface. The pulse-coherent instrument near ADP 3 measured three components of velocity at 4 Hz along three acoustic beams, each beam tilted 25° from vertical (0.025 m vertical rangebins, 0.56 m maximum vertical range). The pulse-coherent instrument collocated with ADP 2 measured only the vertical component of velocity at 8 Hz along a single vertical beam (0.03 m rangebins, 1.1 m maximum range). At ADP 3, significant wave heights Hs and peak periods T_p were calculated from measured 0.05–0.75 Hz pressure fluctuations, using linear wave theory to account for frequency-dependent depth attenuation (Appendix A, Hs estimated as 4 times the standard deviation of the surface elevation). The 0.75-Hz frequency cutoff was chosen to avoid contamination by high-frequency noise, which was magnified when the correction for linear-theory depth attenuation was applied. At ADP 2, depths were greater, depth attenuation was more severe, and pressure measurements were not sufficiently accurate to resolve low-height waves at all frequencies up to 0.75 Hz. To overcome this difficulty, lower-noise estimates of wave heights at ADP 2 were calculated from the cross spectrum between pressure and vertical velocity (Appendix A). During 2009, wave-energy-flux directions were calculated from co-spectra between pressure and horizontal velocity integrated over 0.05–0.75 Hz (using linear theory to account for depth dependence). During 2008, the single vertical beam did not resolve horizontal velocities, preventing calculation of wave directions.

Winds were measured using a Hobo Onset windspeed and direction sensor deployed on 5.5-m-high rock outcrop in 2008, and 4.2 m above the tidal flats in 2009 (open and filled squares, Fig. 1c). Minutely winds were filtered with a 4-min moving average. The wind stress was calculated by assuming a logarithmic profile beneath the windspeed sensor, using a roughness calculated from the significant wave height as (Donelan et al., 1993)

$$z_0 = 6.7 \times 10^{-4}(Hs/4)(|\mathbf{u}_{\text{wind}}|/c)^{2.6}, \tag{19}$$

where $\mathbf{u}_{\text{wind}} =$ 16-min-averaged windspeed, and vertical bars ($|\cdot|$) denote magnitude (similar results were obtained using a constant air-side drag coefficient of 2×10^{-3}). Separations between ADPs and weather stations (about 200 m in 2009 and 570 m in 2008) were smaller than wind decorrelation scales (km) measured over the Skagit flats (Raubenheimer et al., 2013). Nevertheless, local topography (especially Craft Island, Fig. 1b) could cause differences between winds over ADPs and winds measured by weather stations. Furthermore, differences between sea surface roughness and the roughness of nearby saltmarsh vegetation (Fig. 1c) could cause departures from Eq. (19) and the assumed logarithmic velocity profile (Savelyev and Taylor, 2005). Departures were likely most severe in 2008, when the weather station was deployed over land.

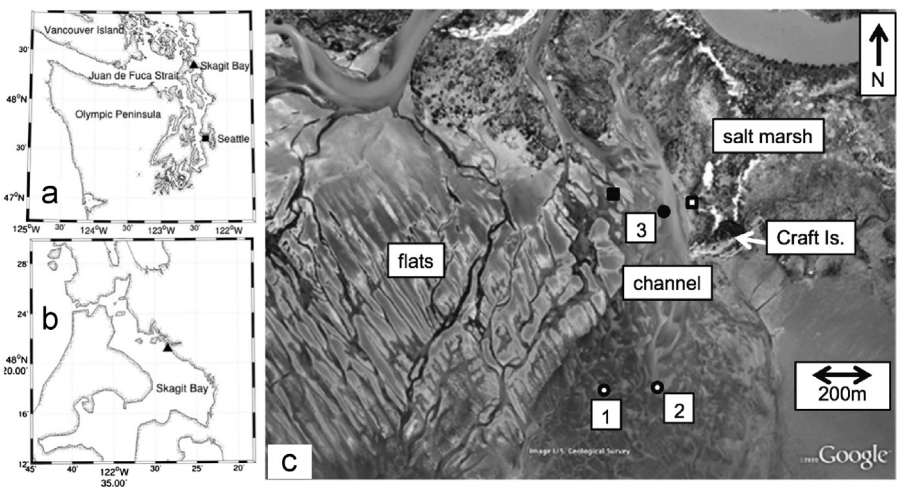

Fig. 1. Maps showing field site location in Puget Sound (triangle, panel a), Skagit Bay (triangle panel b), and image (panel c, source: Google Earth) showing locations of ADPs (circles) and weather stations (squares) from 2008 (open symbols) and 2009 (filled symbols).

Reflections from the sea surface resulted in a region of elevated ADP acoustic backscatter intensity extending up to 0.13 m from the pressure-estimated mean surface elevation. Blurring of reflections away from the mean surface resulted primarily from waves, but also partly from acoustic sidelobes. Velocities measured at the surface closely resembled velocities immediately below the surface, as expected given acoustic reflection from a material surface. Nevertheless, to simplify interpretation, we discarded velocities measured within 0.13 m of the surface. After this selection, in 95% of cases plotted in Figs. 3–7 below, the water surface elevation (estimated from pressure) was more than one significant wave height above the uppermost velocity measurement.

Water velocities were rotated into components u, in the direction of the 4-min-averaged wind velocity, and v, normal to the wind. Every time an ADP rangebin could be found with depth z_1 between 0.13 and 0.2 m beneath the surface, a near-surface value of Δu was calculated from a two-rangebin finite difference: $\Delta u = u(z_1) - u(z_1 + 0.2\ \mathrm{m})$ with $0.13\ \mathrm{m} < z_1 < 0.2\ \mathrm{m}$. For every time, a value of Δu farther from the surface was calculated using a similar finite difference, but with the upper rangebin 0.3–0.4 m from the surface.

4. Results

4.1. Environmental conditions observed during experiment

Wind speeds ranged from 0 to 10 m s^{-1} (Fig. 2a). Afternoon sea breezes were common, blowing towards the southeast (black line, Fig. 2b).

During 2009, the strongest water velocities (up to 0.4 m s^{-1}) flowed roughly north–south (Fig. 2c and d), aligned with the adjacent shoreline and tidal channel (Fig. 1c). Peak flows occurred soon before the flats were drained during ebb tide (dark blue, Fig. 2d), with strong flows also observed soon after the flats were

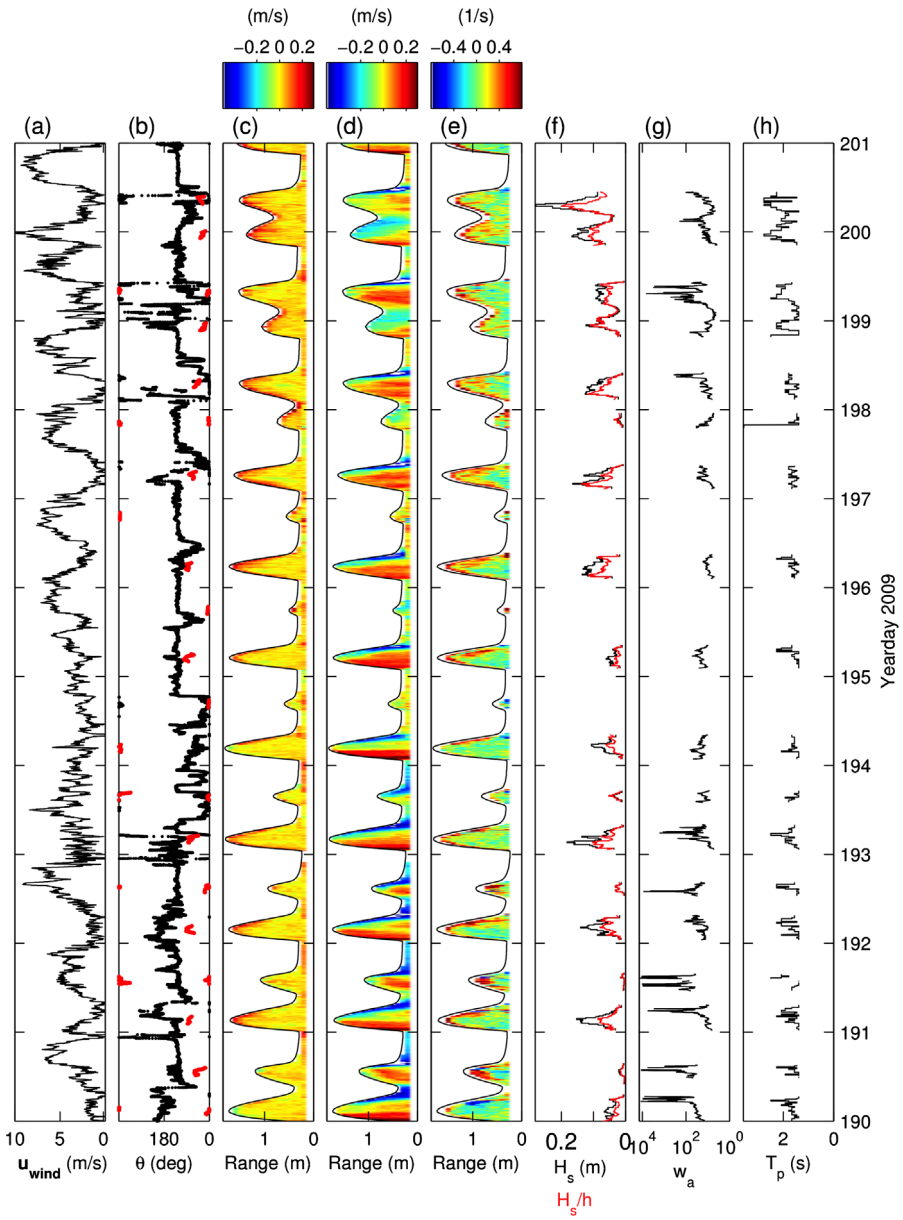

Fig. 2. Experimental conditions from 2009 (instrument 3, Fig. 1). Wind speed (a); wind (black) and wave (red) direction measured clockwise from north (b); eastward (c) and northward (d) water velocity; shear in wind direction (e); significant wave height (Hs, black) and height:depth ratio (Hs/h, red) (f); wave age (g); and peak period T_p (h).

submerged during flood tide (dark red, Fig. 2d), and weak flows around high tide (this trend was also seen in 2008, not shown). In contrast, shear was often strong around high tide, particularly near the water surface (Fig. 2e).

Significant wave heights ranged from 0 to 0.28 m, wave height:depth ratios ranged from 0.05 to 0.2, and waves tended to be largest around high tide (Fig. 2f). Most values of wave age were between 10 and 10^2, although a few ages exceeding 10^3 were observed (Fig. 2g). Peak periods ranged from 1.3 to 4.3 s (Fig. 2h).

4.2. Near-surface shear

To isolate the dependence of shear on wind stress, this section will present only data recorded within 1 h before and after high tide. To minimize influence of the bed, estimates of $\Delta u = u(z_1) - u(z_2)$ are neglected when the depth z_2 of the lower measurement beneath the surface exceeded half of the total water depth. Times of low [$\text{mean}(|\mathbf{u}_{\text{wind}}|) < 1\ \text{m s}^{-1}$] or varying [$\sqrt{\text{var}(u_{\text{wind}}) + \text{var}(v_{\text{wind}})} > 0.1 \times \text{mean}(|\mathbf{u}_{\text{wind}}|)$] winds will be neglected. After this data selection, 9% of high-tide data remained, and 80% of near-surface velocity differences (Δu) were positive in the wind direction, suggesting that much near-surface shear was wind-generated.

Despite the tendency for Δu to be positive in the wind direction, there was no tendency for the velocity difference to increase with wind stress (Fig. 3). This indicates an increase in drag coefficient with windspeed (2), in contrast with the constant drag coefficient predicted by the rigid surface (log-layer) model (6). Since significant wave height was positively correlated with windspeed ($r^2 = 0.81$, not shown), we hypothesize that intense wave-generated mixing prevented development of strong shears under high winds.

The friction velocity (u_*) was correlated with $C_0^{1/2}\Delta u$ (Fig. 4), as predicted by the surface-eddy-viscosity model for wave-enhanced mixing [(2), (8) and (9), $\alpha_0' = 0.14$ chosen to optimize fit]. However, scatter around this trend was substantial. To quantify the error between bin averages and predictions, we define the model skill $S = 1 - \overline{(u_{j,*} - C_j^{1/2}\Delta u_j)^2} / \overline{(u_{j,*}^2)}$, where X_j is the jth bin average of X, and an overbar (–) denotes an average over all data. This skill score measuring model predictions of bin averages was moderately high (0.83, where 1 would indicate a perfect prediction). However, this skill neglects a substantial scatter around bin averages; the standard deviation around the bin averages plotted in Fig. 4 was $2.3 \times 10^{-3}\ \text{m s}^{-1}$, $1.8 \times 10^{-3}\ \text{m s}^{-1}$ and $5.2 \times 10^{-3}\ \text{m s}^{-1}$ for ADPSs 1, 2 and 3, respectively. The two bins that were differenced to calculate Δu had dimensionless depths z_1/Hs and z_2/Hs within the range typical of the WASL (geometric means 4.2 and 9.5, respectively).

The angle θ between waves and winds was large at ADP 3 (compare black and red lines, Fig. 2b), with waves often propagating from the bay to the southwest (0–90°), and with no mean propagation observed away from the nearby shoreline (160–340°). The mean absolute value of θ was 82°, only slightly less than the 90° that would be expected if there were no relationship between wind and wave directions. ADPs 1 and 2 were less sheltered by the shore (Fig. 1), so wind-wave angles might have been smaller, but wave-angle data were unavailable at these locations. Removing from the data set cases where $\theta > 45°$ at ADP 3 slightly improved agreement between remaining observations and predictions of the surface-eddy-viscosity model (Fig. 5, fitted $\alpha_0' = 0.12$). Skill in predicting bin averages was unchanged from the case where angles were neglected ($S = 0.83$), but the standard deviation of ADP 3 measurements around bin averages was reduced from $5.2 \times 10^{-3}\ \text{m s}^{-1}$ in Fig. 4 to $3.1 \times 10^{-3}\ \text{m s}^{-1}$ in

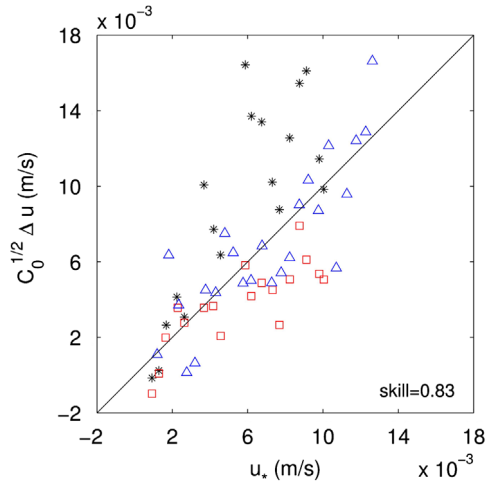

Fig. 4. Friction velocity for wind stress u_* and prediction $C_0^{1/2}\Delta u$ using drag coefficient estimated from the surface-eddy-viscosity model (8) and near-surface Δu measured by ADPs 1 (black stars), 2 (red squares), and 3 (blue triangles). Each point represents mean of all data in a $5 \times 10^{-4}\ \text{m s}^{-1}$ u_* bin, with only means calculated from >5 data points plotted.

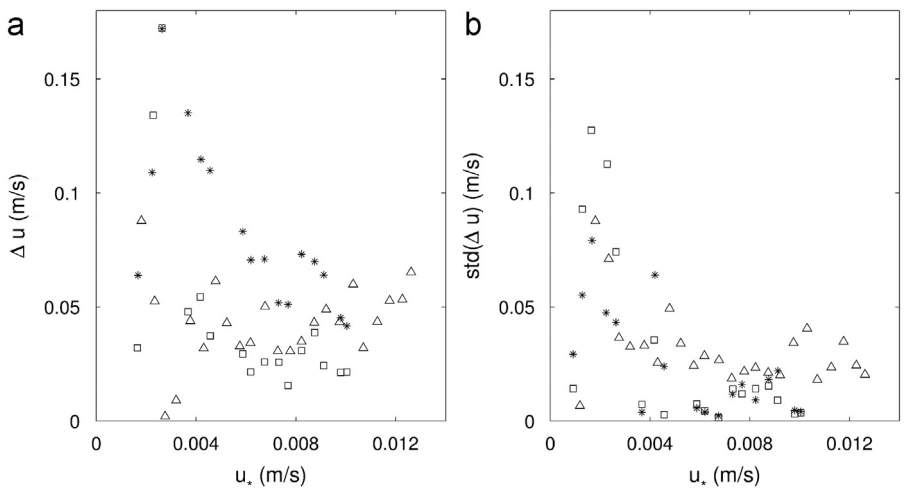

Fig. 3. Near-surface shear Δu versus friction velocity u_* for ADPs 1 (stars), 2 (squares) and 3 (triangles). Each point represents mean (panel a) or standard deviation (panel b) of all data in a $5 \times 10^{-4}\ \text{m s}^{-1}$ u_* bin, with only means calculated from >5 data points plotted. Results not plotted for $u_* < 0.0015\ \text{m s}^{-1}$.

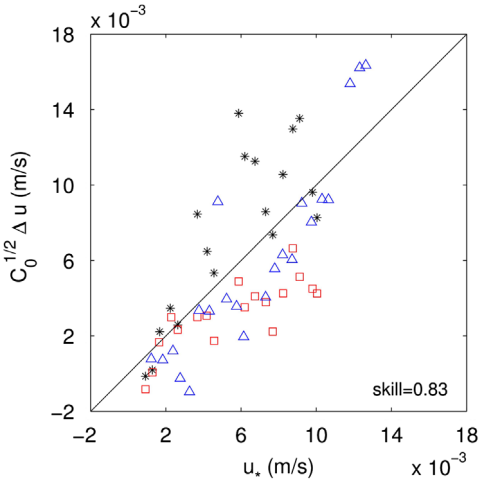

Fig. 5. Similar to Fig. 4, but excluding cases where angle between waves and winds is $>45°$.

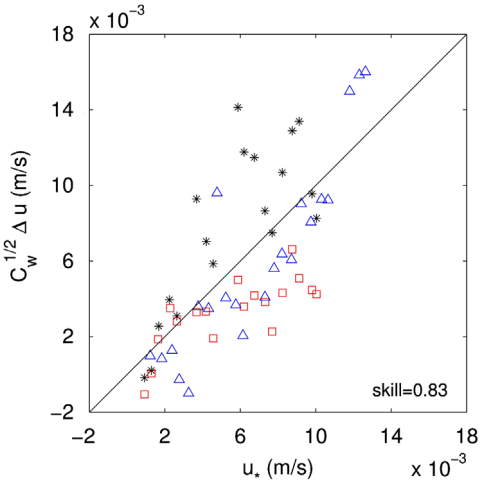

Fig. 6. Similar to Fig. 4, but excluding cases where angle between waves and winds is $>45°$, and using depth-dependent eddy viscosity model (2), (15) and (18).

Fig. 5. The geometric means of dimensionless depths z_1/Hs and z_2/Hs were 5.7 and 13, respectively.

To test for depth-dependence of eddy viscosity, the depth-dependent viscosity model [(2), (15) and (18)] was fitted to data from the three ADPs (Fig. 6). Best fit was obtained with $\alpha'_\nu = 0.12$ and $\beta_\nu = 0.066$, compared with $\alpha'_\nu = 0.3$ and $\beta_\nu = 0.6$ implied by the results of Terray et al. (1999). The small value of the fitted β_ν indicates little variation in eddy viscosity with dimensionless distance from the surface. Predictions of the best-fit depth-dependent eddy viscosity model differed little from surface viscosity model (compare Figs. 5 and 6), skill remained unchanged (S=0.83), and standard deviations around bin averages resembled values for the surface model (2.0×10^{-3} m s^{-1}, 1.6×10^{-3} m s^{-1} and 3.2×10^{-3} m s^{-1} for ADPs 1, 2 and 3, respectively).

The correlations shown in Figs. 4, 5 and 6 are degraded if the condition $\sqrt{\mathrm{var}(u_{\mathrm{wind}}) + \mathrm{var}(v_{\mathrm{wind}})} < 0.1 \times \mathrm{mean}(|\mathbf{u}_{\mathrm{wind}}|)$ is relaxed, indicating that the skill of the simple models tested here is degraded by time-varying winds.

Neither surface nor depth-dependent models provided a good fit to observations at greater depth ($0.3 < z_1 < 0.4$, Fig. 7, fitted $\alpha'_0 = 0.58$, $\alpha'_\nu = 8.0$, $\beta_\nu = -2.2$). The geometric means of dimensionless depths z_1/Hs and z_2/Hs were 8.6 and 14, respectively.

4.3. Estimated eddy viscosity

During the 2009 deployment, fluctuations in wind speeds and wave heights caused large fluctuations in the simulated wave-generated surface eddy viscosity ν_0 (Fig. 8). The simulated surface eddy viscosity reached maximum values $5–10 \times 10^{-4}$ m^2 s^{-1} during cases with relatively strong winds and waves, although neither winds nor waves were very large compared with values often observed in less sheltered environments. Owing to a tendency for wave height to increase with increasing depth, the cases of high simulated surface eddy viscosity tended to occur during the higher tides. The simulations neglect any near-surface mixing resulting from turbulence generated by bottom friction. Furthermore, cases with strong tidal flows, when bottom friction may be large, were excluded from model–data comparisons by the selection of data around high tide. Therefore, the simulated tendency for eddy viscosity to decrease before and after high tide should not be extrapolated to times of strong flood and ebb flows. The simulated eddy viscosity reached minimum values below molecular viscosity ($\sim 1.5 \times 10^{-6}$ m^2 s^{-1}), an unrealistic prediction indicating that, during times of low winds and waves, the simulated wave mixing became so weak that other sources of mixing dominated. These weak-mixing cases had little impact on the fits shown in Figs. 4–7, because both u_* and $C^{1/2}\Delta u$ were nearly zero in these cases.

5. Discussion and conclusions

Models for near-surface mixing were tested against observations of shear near the water surface over a flooded tidal flat. Within 0.4 m of the surface, shear was usually positive in the downwind direction, suggesting that much of the shear was wind-generated. However, contrary to the predictions of a model that neglects wave-generated mixing, observed shear did not tend to increase with increasing windspeed. Simulations of near-surface mixing by waves were roughly consistent with the observed relationship between shear and windspeed, although scatter around predictions was substantial. Simulated wave mixing increased with windspeed, preventing development of strong near-surface shears under strong winds.

Consistent with previous observations of near-surface turbulence (Jones and Monismith, 2008), these results suggest that wave-generated mixing may play an important role in controlling near-surface shear, even in sheltered estuaries under moderate (1–10 m s^{-1}) winds. Near-surface shear, and associated dispersion, might influence the spreading of thin freshwater plumes, or the transport of buoyant organisms and pollutants (Elliot, 1986).

Simulated wave-generated near-surface eddy viscosity ranged from negligible (below molecular viscosity) when winds and waves were weak to $5–10 \times 10^{-4}$ m^2 s^{-1} when winds and waves were relatively strong. Owing to a tendency for wave height to increase with increasing depth, the cases of high simulated surface eddy viscosity tended to occur during the higher tides.

The substantial scatter around the predictions of the wind-forced, wave-mixed model might be explained by model deficiencies, by deficiencies in wind stress estimates (Section 3), or by the shallow (<0.5 m thick) freshwater plumes observed at this location (Mullarney and Henderson, 2011).

The models for wave-enhanced near-surface mixing that we tested were based on models developed by previous researchers to explain observations of enhanced near-surface turbulent dissipation. These models assumed a balance between generation of waves by winds and dissipation of turbulent energy. The angle θ between wave propagation and wind direction can influence wave generation (Donelan, 1999), an effect neglected in the

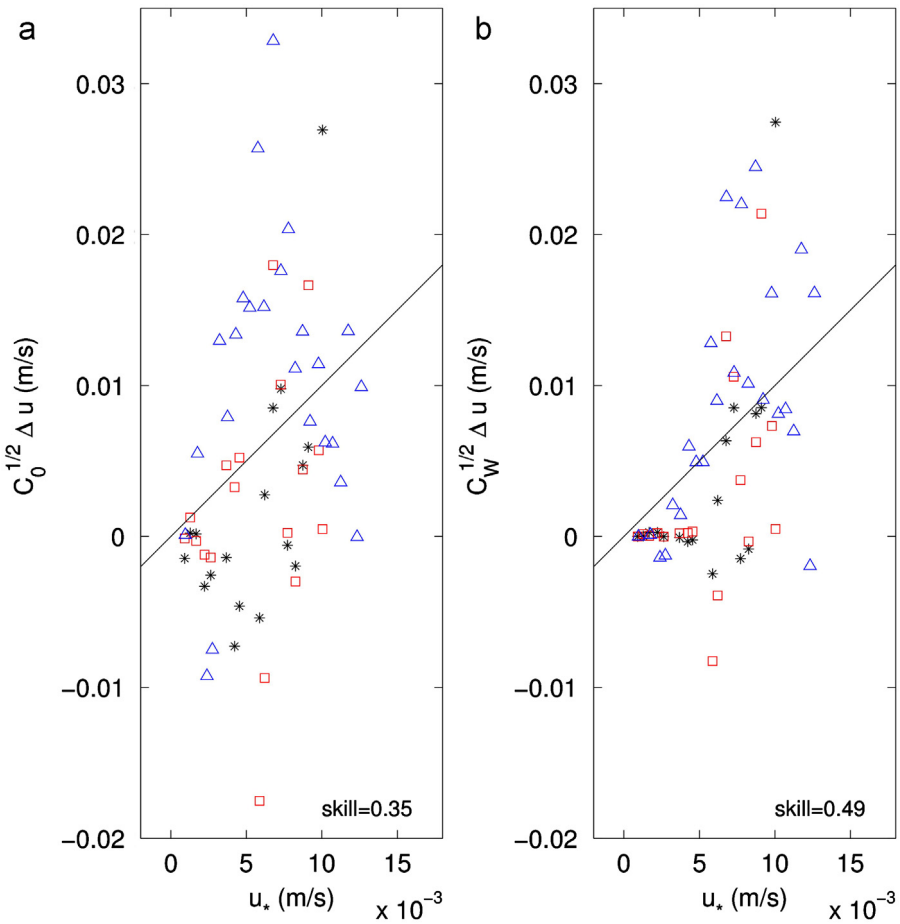

Fig. 7. Similar to Fig. 4, but using shear at depth (upper bin 0.3–0.4 m beneath surface), and comparing surface [panel (a), Eq. (7)] and depth-dependent [panel b, Eqs. (2), (15), (18)] eddy-viscosity models.

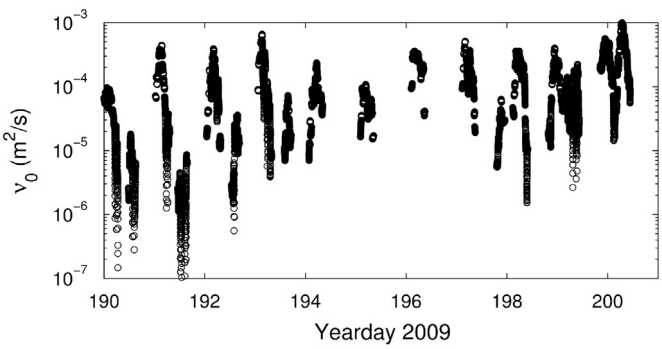

Fig. 8. Surface eddy viscosity (ν_0) predicted by model (7) for 2009 deployment.

models. In the cases presented here, sheltering by nearby marshes yielded numerous cases of large wind-wave angles (mean absolute value of $\theta = 82°$). Scatter around model predictions was slightly reduced when cases with moderate or large angles ($\theta > 45°$) were removed from the data set.

The fitted near-surface (0.13 m $< z_1 <$ 0.2 m) eddy viscosity increased weakly with increasing depth as $\zeta^{0.07}$ (ζ is the depth beneath the surface divided by wave height), slower than the $\zeta^{0.6}$ implied by the model of Terray et al. (1999). Owing to this weak depth-dependence, simply fitting a surface eddy viscosity instead of a depth-dependent value yielded only a minor reduction in model skill. At greater depths (0.3 m $< z_1 <$ 0.4 m), the models for wind-generated shear had little skill predicting the observed shear, suggesting that shear at depth may have been forced by factors other than the wind stress, such as tidal currents or spreading of freshwater plumes.

Acknowledgments

We thank Kassi Riffe, Chris Eager, and Nate Raynor for assistance with the field work. Funding was provided by the Office of Naval Research and the State of Washington.

Appendix A. Estimation of wave height and period

The sea-surface elevation fluctuation η is related to pressure p and vertical velocity w at depths z_p and z_w beneath the surface by

$$\langle \eta \rangle_\sigma = \Gamma_{p,\sigma} \langle p \rangle_\sigma, \tag{A.1}$$

$$\langle \eta \rangle_\sigma = \Gamma_{w,\sigma} \langle w \rangle_\sigma, \tag{A.2}$$

where $\langle X \rangle_\sigma$ is the frequency–σ complex amplitude of X, the linear theory transfer functions are

$$\Gamma_{p,\sigma} = \frac{\cosh(kh)}{\cosh[k(h-z_p)]}, \tag{A.3}$$

$$\Gamma_{w,\sigma} = -\frac{i \sinh(kh)}{\sigma \sinh[k(h-z_w)]}, \tag{A.4}$$

h is the total water depth, and the wavenumber k is calculated from the linear dispersion relation $\sigma^2 = gk \tanh(kh)$ (Phillips, 1977).

The significant wave height is calculated form the sea-surface variance, which is the sum of $|\langle\eta\rangle_\sigma|^2$ over all wave frequencies (0.05–0.75 Hz). From Eq. (A.1), $|\langle\eta\rangle_\sigma|^2$ can be estimated from pressure as $|\Gamma_{p,\sigma}\langle p\rangle_\sigma|^2$. This estimate is biased high, because noise in measured pressure is squared. From (A.1) and (A.2) (assuming noise in pressure and velocity are uncorrelated), an unbiased estimate of $|\langle\eta\rangle_\sigma|^2$ is $\Re\{\Gamma_{p,\sigma}\Gamma^*_{w,\sigma}\langle p\rangle_\sigma\langle w\rangle^*_\sigma\}$, where * denotes a complex conjugate and $\Re$ denotes the real part. Errors in the unbiased estimate become small if many degrees of freedom are used, although this advantage is partly offset by the higher noise of the velocity measurements. At frequencies much above 0.75 Hz, depth attenuation became so severe during the highest tides that errors dominated even the unbiased estimates, often leading to negative $|\langle\eta\rangle_\sigma|^2$ estimates. We used 50 degrees of freedom when calculating peak periods, whereas significant wave heights used band-integrated spectra, resulting in many more degrees of freedom. We further reduced noise by averaging multiple estimates of $|\langle\eta\rangle_\sigma|^2$ obtained from multiple rangebins of the pulse-coherent ADP. We discarded w measured <0.2 m beneath the surface, and then averaged estimates from the highest 10 remaining rangebins between 0.35 m and 1.1 m above the bed.

References

Anis, A., Moum, J., 1992. The superadiabatic surface layer of the ocean during convection. Journal of Physical Oceanography 22, 1221–1227.

Burchard, H., 2001. Simulating the wave-enhanced layer under breaking surface waves with two-equation turbulence models. Journal of Physical Oceanography 31, 3133–3145.

Craig, P.D., Banner, M.L., 1994. Modeling wave-enhanced turbulence in the ocean surface layer. Journal of Physical Oceanography 24, 2546–2559.

Donelan, M., 1998. Physical processes in lakes and oceans. In: Air–Water Exchange Processes. American Geophysical Union. pp. 19–36.

Donelan, M., 1999. Wind-induced growth and attenuation of laboratory waves. In: Wind-over-Wave Couplings. Perspective and Prospects. Oxford. pp. 183–194.

Donelan, M., Dobson, F., Smith, S., Anderson, R., 1993. On the dependence of sea surface roughness on wave development. Journal of Physical Oceanography 23, 2143–2149.

Drennan, W., Kahma, K., Terray, E., Donelan, M., Kitaigorodskii, S., 1992. Observations of the enhancement of kinetic energy dissipation beneath breaking wind waves. In: Breaking Waves. Springer. pp. 95–101.

Elliot, A., 1986. Shear diffusion and the spread of oil in the surface layers of the north sea. Ocean Dynamics 39, 117–137.

Feddersen, F., Trowbridge, J., Williams, A., 2007. Vertical structure of dissipation in the nearshore. Journal of Physical Oceanography 37, 1764–1777.

Gemmrich, J., Farmer, D., 2004. Near-surface turbulence in the presence of breaking waves. Journal of Physical Oceanography 34, 1067–1086.

Gerbi, G., Trowbridge, J., Edson, J., Plueddemann, A., Terray, E., 2008. Measurements of momentum and heat transfer across the air–sea interface. Journal of Physical Oceanography 38, 1054–1072.

Gerbi, G., Trowbridge, J., Terray, E., Plueddemann, A., Kukulka, A., 2009. Observations of turbulence in the ocean surface boundary layer: energetics and transport. Journal of Physical Oceanography 39, 1077–1096.

Jones, N.L., Monismith, S.G., 2008. The influence of whitecapping waves on the vertical structure of turbulence in a shallow estuarine embayment. Journal of Physical Oceanography 38, 1563–1580.

Kitaigorodskii, S., Donelan, M., Lumley, J., Terray, E., 1983. Wave–turbulence interactions in the upper ocean. Part II. Statistical characteristics of wave and turbulent components of the random velocity field in the marine surface layer. Journal of Physical Oceanography 555, 1988–1999.

Melville, W., 1996. The role of surface-wave breaking in air–sea interaction. Journal of Fluid Mechanics 28, 279–321.

Mullarney, J.C., Henderson, S.M., 2011. Hydraulically-controlled front trapping on a tidal flat. Journal of Geophysical Research 116 http://dx.doi.org/10.1029/2010JC006520.

Phillips, O., 1977. The Dynamics of the Upper Ocean, second ed. Cambridge University Press.

Raubenheimer, B., Ralston, D., Elgar, S., Griffen, D., Signell, R., 2013 Observations and predictions of summertime winds on the Skagit tidal flats, Washington. Continental Shelf Research 60S, S13–S21.

Savelyev, S.A., Taylor, P.A., 2005. Internal boundary layers. I. Height formulae for neutral and diabatic flows. Boundary Layer Meteorology 115, 1–25.

Stacey, M., 1999. Simulation of the wind-forced near-surface circulation in Knight Inlet: a parameterization of the roughness length. Journal of Physical Oceanography 29, 1363–1367.

Stacey, M., Pond, S., 1997. On the Mellor–Yamada turbulence closure scheme: the surface boundary condition for q^2. Journal of Physical Oceanography 27, 2081–2086.

Tennekes, H., Lumley, J., 1972. A First Course in Turbulence. MIT Press.

Terray, E., Donelan, M., Agrawal, Y., Drennan, W., Kahma, K., Williams, A., Hwang, P., Kitaigorodskii, S., 1996. Estimates of kinetic energy dissipation under breaking waves. Journal of Physical Oceanography 26, 792–807.

Terray, E., Drennan, W., Donelan, M., 1999. The vertical structure of shear and dissipation in the ocean surface layer. In: Banner, M. (Ed.), The Wind-Driven Air–Sea Interface. New South Wales. pp. 239–245.

Thorpe, S., 2004. Langmuir circulation. Annual Reviews of Fluid Mechanics 36, 55–79.